



A Nonlinear Thermomechanical Model of Spinel Ceramics Applied to Aluminum Oxynitride (ALON)

by John D. Clayton

ARL-RP-309

January 2011

A reprint from the Journal of Applied Mechanics, Vol. 78, pp. 011013-1–011013-11, January 2011.

NOTICES

Disclaimers

The findings in this report are not to be construed as an official Department of the Army position unless so designated by other authorized documents.

Citation of manufacturer's or trade names does not constitute an official endorsement or approval of the use thereof.

DESTRUCTION NOTICE—For classified documents, follow the procedures in DOD 5220.22-M, National Industrial Security Program Operating Manual, Chapter 5, Section 7, or DOD 5200.1-R, Information Security Program Regulation, C6.7. For unclassified, limited documents, destroy by any method that will prevent disclosure of contents or reconstruction of the document.

Army Research Laboratory

Aberdeen Proving Ground, MD 21005-5069

ARL-RP-309**January 2011**

A Nonlinear Thermomechanical Model of Spinel Ceramics Applied to Aluminum Oxynitride (ALON)

John D. Clayton
Weapons and Materials Research Directorate, ARL

A reprint from the *Journal of Applied Mechanics*, Vol. 78, pp. 011013-1–011013-11, January 2011.

REPORT DOCUMENTATION PAGE				Form Approved OMB No. 0704-0188	
Public reporting burden for this collection of information is estimated to average 1 hour per response, including the time for reviewing instructions, searching existing data sources, gathering and maintaining the data needed, and completing and reviewing the collection information. Send comments regarding this burden estimate or any other aspect of this collection of information, including suggestions for reducing the burden, to Department of Defense, Washington Headquarters Services, Directorate for Information Operations and Reports (0704-0188), 1215 Jefferson Davis Highway, Suite 1204, Arlington, VA 22202-4302. Respondents should be aware that notwithstanding any other provision of law, no person shall be subject to any penalty for failing to comply with a collection of information if it does not display a currently valid OMB control number. PLEASE DO NOT RETURN YOUR FORM TO THE ABOVE ADDRESS.					
1. REPORT DATE (DD-MM-YYYY) January 2011		2. REPORT TYPE Reprint		3. DATES COVERED (From - To) October 2009–October 2010	
4. TITLE AND SUBTITLE A Nonlinear Thermomechanical Model of Spinel Ceramics Applied to Aluminum Oxynitride (AION)				5a. CONTRACT NUMBER	
				5b. GRANT NUMBER	
				5c. PROGRAM ELEMENT NUMBER	
6. AUTHOR(S) John D. Clayton				5d. PROJECT NUMBER AH80	
				5e. TASK NUMBER	
				5f. WORK UNIT NUMBER	
7. PERFORMING ORGANIZATION NAME(S) AND ADDRESS(ES) U.S. Army Research Laboratory ATTN: RDRL-WMP-B Aberdeen Proving Ground, MD 21005-5069				8. PERFORMING ORGANIZATION REPORT NUMBER ARL-RP-309	
9. SPONSORING/MONITORING AGENCY NAME(S) AND ADDRESS(ES)				10. SPONSOR/MONITOR'S ACRONYM(S)	
				11. SPONSOR/MONITOR'S REPORT NUMBER(S)	
12. DISTRIBUTION/AVAILABILITY STATEMENT Approved for public release; distribution is unlimited.					
13. SUPPLEMENTARY NOTES A reprint from the <i>Journal of Applied Mechanics</i> , Vol. 78, pp. 011013-1–011013-11, January 2011.					
14. ABSTRACT A continuum model is developed for describing deformation and failure mechanisms in crystalline solids (ceramics and minerals) with the cubic spinel structure. The constitutive model describes the response under conditions pertinent to impact loading: high pressures, high strain rates, and, possibly, high temperatures. Nonlinear elasticity, anisotropy, thermoelastic coupling, dislocation glide, twinning, shear-induced fracture, and pressure-induced pore collapse are addressed. The model is applied to enable an improved understanding of transparent ceramic aluminum oxynitride (AION). Calculations demonstrate an accurate depiction of hydrostatic and shear stresses observed experimentally in shockloaded polycrystalline AION. Various choices of initial resistances to slip, twinning, or shear fracture that result in similar predictions for average stresses in polycrystals but different predictions for defect densities (accumulated dislocations and twin volume fractions) are investigated. Predictions for single crystals provide insight into grain orientation effects not available from previous experimental investigations.					
15. SUBJECT TERMS elasticity, plasticity, shock physics, ceramics, minerals, AION					
16. SECURITY CLASSIFICATION OF:			17. LIMITATION OF ABSTRACT UU	18. NUMBER OF PAGES 18	19a. NAME OF RESPONSIBLE PERSON John Clayton
a. REPORT Unclassified	b. ABSTRACT Unclassified	c. THIS PAGE Unclassified			19b. TELEPHONE NUMBER (Include area code) 410-278-6146

A Nonlinear Thermomechanical Model of Spinel Ceramics Applied to Aluminum Oxynitride (AlON)

J. D. Clayton

Mem. ASME
Impact Physics,
US Army Research Laboratory,
Aberdeen Proving Ground,
MD 21005-5066
e-mail: jclayton@arl.army.mil

A continuum model is developed for describing deformation and failure mechanisms in crystalline solids (ceramics and minerals) with the cubic spinel structure. The constitutive model describes the response under conditions pertinent to impact loading: high pressures, high strain rates, and, possibly, high temperatures. Nonlinear elasticity, anisotropy, thermoelastic coupling, dislocation glide, twinning, shear-induced fracture, and pressure-induced pore collapse are addressed. The model is applied to enable an improved understanding of transparent ceramic aluminum oxynitride (AlON). Calculations demonstrate an accurate depiction of hydrostatic and shear stresses observed experimentally in shock-loaded polycrystalline AlON. Various choices of initial resistances to slip, twinning, or shear fracture that result in similar predictions for average stresses in polycrystals but different predictions for defect densities (accumulated dislocations and twin volume fractions) are investigated. Predictions for single crystals provide insight into grain orientation effects not available from previous experimental investigations.

[DOI: 10.1115/1.4002434]

Keywords: elasticity, plasticity, shock physics, ceramics, minerals, AlON

1 Introduction

At standard temperature and pressure, many ceramic crystals and crystalline minerals, e.g., corundum (α - Al_2O_3), quartz (α - SiO_2), moissanite ($6H$ - SiC), and diamond, are hard, brittle, and elastically stiff and often exhibit a predilection toward fracture over dislocation glide or deformation twinning. However, at high temperatures or high pressures, dislocation glide or twinning can be important [1,2]. Confining pressures, for example, those occurring in impact loading or indentation, can partially or fully suppress fracture [3–5].

The theory developed in the present paper addresses behavior of such materials in regimes wherein nonlinear thermoelastic properties as well as inelastic deformation modes may be of importance. The constitutive model developed in this paper is directed toward cubic Bravais lattices and centrosymmetric structures. For example, spinel ceramics, such as MgAl_2O_4 and aluminum oxynitride (AlON), belong to point groups with cubic symmetry and centrosymmetry [6]. The general framework developed here applies to any crystal with such symmetries exhibiting the following physics: hyperelasticity, thermal expansion, slip, twinning, and shear stress-induced fracture. The particular application is a study of AlON, a transparent ceramic known to exhibit dislocation glide and twinning mechanisms when subjected to confined compressive loading at high strain rates [4,7]. Dislocation glide has been observed in other ceramics sharing the spinel structure (e.g., stoichiometric variations of $\text{MgO}-n\text{Al}_2\text{O}_3$, $1 \leq n \leq 3.5$) at various confining pressures and temperatures [8,9].

Because single crystals of AlON cannot presently be obtained using standard processing routes, they have not been mechanically tested. Anisotropic second-order elastic constants for AlON have, however, been recently computed theoretically via first principles,

i.e., quantum mechanics [10]. Polycrystalline AlON has been extensively tested and characterized [7,11,12]. Polycrystals exhibit typical grain sizes of 20–200 μm with minor porosity (1–5%, often near-spherical pores of diameter 1–15 μm) and impurities often located preferentially along grain boundaries [7,13]. Results presented later in this paper demonstrate how a model incorporating nonlinear thermoelasticity and pore collapse can explain the hydrostatic (pressure-volume) response of shock-loaded polycrystalline AlON to pressures up to ~ 30 GPa and suggest how slip, twinning, and shear fracture may contribute to the deviatoric (i.e., shear stress-distortion) mechanical response. The model developed here may be used later in mesoscale calculations of deformation and failure of polycrystalline microstructures [14,15].

This paper is organized as follows. Section 2 describes a general constitutive model framework for cubic ceramic crystals and minerals exhibiting a center of symmetry. Section 3 specializes the model to single crystals of AlON and includes a compilation of thermomechanical properties and properties of lattice defects such as full and partial dislocations and deformation twins. Properties are obtained via theoretical considerations (e.g., the Peierls–Nabarro model or anisotropic elasticity [16,17]) when experimental data are absent. These computed defect properties have not been reported elsewhere. Section 4 develops an averaging scheme to predict the response of polycrystals with random initial lattice orientations and initial porosity, incorporating treatment of reduction in elastic coefficients of the macroscopically isotropic aggregate using a self-consistent approach, pore collapse at high pressures [18,19], and possible fracture induced by shear stresses at grain boundaries or other defects. Discussed are predictions of the response of polycrystals to hydrostatic compression and of polycrystals and single crystals of several orientations to uniaxial strain loading under adiabatic conditions at a high strain rate. The latter set of loading conditions is representative of plate impact experiments on single crystals and polycrystals [2,12,20–23]. Comparisons with experimental data on polycrystals [12,24–27] are included; results for single crystals are limited to predictions because single crystal experimental data are not available.

Contributed by the Applied Mechanics Division of ASME for publication in the JOURNAL OF APPLIED MECHANICS. Manuscript received December 10, 2009; final manuscript received August 17, 2010; accepted manuscript posted August 24, 2010; published online October 20, 2010. Assoc. Editor: Horacio D. Espinosa.

Terminology and notation of nonlinear continuum mechanics are used. Vectors and tensors are written in indicial notation in Cartesian coordinates. Repeated subscripted indices are summed. Superposed -1 and \bullet denote inversion and material time differentiation, respectively.

2 Nonlinear Model for Cubic Single Crystals

Let $x_a = x_a(X_A, t)$ denote the spatial coordinates that depend on reference coordinates X_A of a material particle and time t . The deformation gradient F_{aA} is decomposed into elastic ($F_{a\alpha}^E$) and plastic ($F_{a\alpha}^P$) parts as [28,29]

$$F_{aA} = \partial_A x_a = F_{a\alpha}^E F_{a\alpha}^P \quad (1)$$

with $\partial_A(\cdot) = \partial(\cdot)/\partial X_A = F_{aA} \partial_a(\cdot)$. Denote by $v_a = \dot{x}_a$ the particle velocity. The spatial velocity gradient is

$$L_{ab} = \partial_b \dot{x}_a = \partial_b v_a = \dot{F}_{aA} F_{Ab}^{-1} = \dot{F}_{a\alpha}^E F_{\alpha b}^{E-1} + F_{a\alpha}^E L_{\alpha\beta}^P F_{\beta b}^{E-1} \quad (2)$$

The total plastic velocity gradient results from dislocation glide and deformation twinning:

$$L_{\alpha\beta}^P = \dot{F}_{\alpha\beta}^P F_{\alpha\beta}^{P-1} = \sum_i \dot{\gamma}^i s_\alpha^i m_\beta^i + \sum_j \dot{f}^j \gamma^j s_\alpha^j m_\beta^j \quad (3)$$

In Eq. (3), the set $\{\dot{\gamma}^i, s_\alpha^i, m_\beta^i\}$ denotes {shearing rate, slip direction, and slip plane normal} for slip system i and the set $\{\dot{f}^j, \gamma^j, s_\alpha^j, m_\beta^j\}$ denotes {volume fraction rate, fixed twinning shear, shear direction, and habit plane normal} for twin system j . The total volume fraction of twinned crystal is $f_T = \sum_j f^j$. A comprehensive treatment of kinematics of crystal plasticity models incorporating twinning is given elsewhere [2]. Since s and m are orthogonal for each i or j , volume is unchanged by plastic deformation: $\dot{J}^P = d(\det F^P)/dt = J^P L_{\alpha\alpha}^P = 0$. Local mass conservation results in $\rho_0 = \rho J^E$, where ρ_0 is the reference mass density, ρ is the spatial mass density, and $J^E = \det F^E$.

Denote by θ the absolute temperature and by $E_{\alpha\beta}^E = (F_{a\alpha}^E F_{a\beta}^E - \delta_{\alpha\beta})/2$ the finite elastic strain tensor with $\delta_{\alpha\beta}$ Kronecker's delta. Helmholtz free energy per unit mass $\psi(E_{\alpha\beta}^E, \theta, \rho_D, \eta_T)$ is prescribed as

$$\rho_0 \psi = \frac{1}{2} C_{\alpha\beta\chi\delta} E_{\alpha\beta}^E E_{\chi\delta}^E + \frac{1}{6} C_{\alpha\beta\chi\delta\epsilon\phi} E_{\alpha\beta}^E E_{\chi\delta}^E E_{\epsilon\phi}^E - \beta E_{\alpha\alpha}^E (\theta - \theta_0) - \rho_0 c_V \theta \log \frac{\theta}{\theta_0} + \frac{1}{2} \Lambda P_A P_A + \hat{K} b^2 \rho_D + \frac{1}{2} \bar{\gamma} \eta_T \quad (4)$$

The second- and third-order elastic coefficients are $C_{\alpha\beta\chi\delta}$ and $C_{\alpha\beta\chi\delta\epsilon\phi}$, respectively; these coefficients may depend on temperature in Eq. (4). In cubic crystals of Laue group CI [30–32], independent second-order coefficients in Voigt's notation are C_{11} , C_{12} , and C_{44} and independent third-order coefficients are C_{111} , C_{112} , C_{123} , C_{144} , C_{155} , and C_{456} . The isochoric specific heat per unit mass is c_V and θ_0 is a constant. The thermal stress coefficient β satisfies

$$\beta = 3\alpha_T B = \rho_0 \Gamma c_V \quad (5)$$

with B as the isothermal bulk modulus ($B = (C_{11} + 2C_{12})/3$ at null elastic strain), α_T as the coefficient of thermal expansion, and Γ as the Gruneisen's parameter. Denoting by c_P the isobaric specific heat and B_η the isentropic bulk modulus, the following identity applies [30]:

$$c_P/c_V = B_\eta/B = 1 + 3\alpha_T \Gamma \theta \quad (6)$$

Isothermal shear moduli $(C_{11} - C_{12})/2$ and C_{44} are equal to their isentropic counterparts in cubic crystals. The reference electric polarization vector is $P_A = F_{aA} p_a$ [33] with p_a as the spatial polarization per unit volume. The material constant Λ satisfies [34,35]

Table 1 Structural features of γ -AlON

Feature	Value	Remarks	Reference
Composition	Al ₂₃ O ₂₇ N ₅	35.7 mol % AlN	[39]
Crystal structure	Spinel	Cubic	[6]
Space group	Fd3m	No. 227	
Point group	m3m	Centrosymmetric	
Lattice parameter	7.952 Å	Room temperature	[13]

$$\Lambda = 1/[\epsilon_0(\epsilon - 1)] \quad (7)$$

with ϵ_0 as the vacuum permittivity and ϵ as the static dielectric constant. In centrosymmetric crystals, piezoelectric and pyroelectric effects do not appear. Electrostrictive constants unknown for the material of subsequent interest (i.e., AlON) are omitted. The rightmost two terms in Eq. (4) account for energies of lattice defects. The scalar dislocation density (length per unit volume) is ρ_D and the scalar twin boundary density (area per unit volume) is η_T . Scalar b denotes the magnitude of a typical Burgers vector, \hat{K} is an energy factor that depends on elastic constants and dislocation type [16], and $\bar{\gamma}$ is the stacking fault energy presumed twice the energy per unit area associated with twin boundaries [2,17].

The elastic second Piola–Kirchhoff stress $S_{\alpha\beta}$ and Cauchy stress σ_{ab} are obtained from Eq. (4) as

$$S_{\alpha\beta} = J^E F_{a\alpha}^{E-1} \sigma_{ab} F_{\beta b}^{E-1} = \rho_0 \frac{\partial \psi}{\partial E_{\alpha\beta}^E} = C_{\alpha\beta\chi\delta} E_{\chi\delta}^E + \frac{1}{2} C_{\alpha\beta\chi\delta\epsilon\phi} E_{\chi\delta}^E E_{\epsilon\phi}^E - \beta(\theta - \theta_0) \delta_{\alpha\beta} \quad (8)$$

Maxwell's stress of nonlinear electromechanics [33] is omitted in Eq. (8) since applications considered later do not involve electrodynamics or strong electric fields. After applying thermodynamic arguments [2,23,31], the local balance of energy can be expressed as

$$\rho_0 c_V \dot{\theta} = k \nabla^2 \theta + \rho_0 r + \sum_i \tau^i \dot{\gamma}^i + \sum_j \tau^j \dot{f}^j \gamma^j - \theta \beta \dot{E}_{\alpha\alpha}^E - \left(\hat{K} - \theta \frac{\partial \hat{K}}{\partial \theta} \right) b^2 \dot{\rho}_D - \frac{1}{2} \bar{\gamma} \dot{\eta}_T \quad (9)$$

with k as the thermal conductivity, r as an external heat supply, and the resolved shear stresses

$$\tau^i = J^E F_{a\alpha}^E s_\alpha^i \sigma_{ab} m_\beta^i F_{\beta b}^{E-1}, \quad \tau^j = J^E F_{a\alpha}^E s_\alpha^j \sigma_{ab} m_\beta^j F_{\beta b}^{E-1} \quad (10)$$

Kinetic equations for slip and twinning are prescribed as [2]

$$\dot{\gamma}^i = \dot{\gamma}_0 |\tau^i / \tau_C^i|^m \text{sgn}(\tau^i), \quad \dot{f}^j = \begin{cases} (\dot{\gamma}_0 / \gamma^j) |\tau^j / \tau_C^j|^n & [\tau^j > 0 \text{ and } f_T < 1] \\ 0 & [\tau^j \leq 0 \text{ or } f_T = 1] \end{cases} \quad (11)$$

where $\dot{\gamma}_0$ is a constant, m and n are the rate sensitivities, and τ_C^i and τ_C^j are the slip and twin resistances that can evolve with the thermodynamic state as well as activity of all slip and twin systems. Conditions in the second of Eq. (11) require that the rate of twin volume fraction is non-negative (stress-induced detwinning is not considered) and that the total volume fraction of twinned crystal $f_T \leq 1$.

3 Aluminum Oxynitride: Thermoelastic Properties and Lattice Defects

Structural parameters for AlON with supporting references are listed in Table 1. Thermophysical properties are listed in Table 2; many follow from a review paper [11], which, in turn, lists a number of sources. Elastic properties are listed in Table 3. Because only isotropic polycrystalline values are available for pressure- and temperature-derivatives of elastic coefficients [13],

Table 2 Thermophysical properties (at room temperature θ_0 unless noted otherwise)

Parameter	Value	Definition	Reference
ρ_0	3714 kg/m ³	Mass density	[13]
c_p	708+2.32($\theta-\theta_0$) J/kg K	Isobaric specific heat	[11]
α_T	5.23×10^{-6} /K	Thermal expansion	[11]
k	10.89 W/m K	Thermal conductivity	[11]
ϵ	8.5	Dielectric constant (at 10 ² Hz)	[11]
θ_M	2165 K	Melting temperature	[11]
Γ_0	1.28	Gruneisen parameter	Eq. (5)

such derivatives of second-order elastic coefficients are estimated in model calculations from isotropic results via $C'_{11}-C'_{12}=2C'_{44}$, where primes denote a partial derivative with respect to temperature or pressure. Third-order coefficients have not been measured experimentally but can be estimated, in part, from pressure derivatives of second-order coefficients omitting dependence of elastic coefficients on shear strains [23]:

$$C_{\alpha\beta\chi\delta\epsilon\phi} = -(B/3)[(\partial C_{\alpha\beta\chi\delta}/\partial p)\delta_{\epsilon\phi} + (\partial C_{\epsilon\phi\alpha\beta}/\partial p)\delta_{\chi\delta} + (\partial C_{\chi\delta\epsilon\phi}/\partial p)\delta_{\alpha\beta}] \quad (12)$$

Dislocations are addressed in Table 4: Full 1/2<110> and partial 1/4<110> dislocations are considered. Line energy W (full and partial dislocations) and Peierls–Nabarro stress τ_{PN} (full dislocations only) are calculated analytically [16] via

$$W = [\hat{K}b^2/(4\pi)]\log(R/R_0) \approx \hat{K}b^2, \quad \tau_{PN} = 2\hat{K} \exp[-2\pi(\hat{K}/\hat{\mu}) \times (d/b)] \quad (13)$$

where R is the distance from the dislocation line, R_0 is the core radius, $\hat{\mu}$ is the appropriate shear elastic constant (see Appendix), d is the spacing between slip planes, and \hat{K} depends on the second-order elastic coefficients and the geometry of the dislocation line. Partial dislocations on {111} planes have been observed in dynamically compressed AlON [4]. Slip on {110} planes is also considered in Table 4 since near room temperatures, Veyssiere et al. [8] found slip resistance on {110} planes to be lower than that on {111} in MgO– n Al₂O₃ spinel ($n \sim 1.1$) single crystals. On the other hand, MgO– n Al₂O₃ spinel ($n \sim 3.5$) exhibited a lower re-

Table 3 Elastic properties

Parameter	Value	Definition	Reference
C_{11}	377 GPa	Second-order elastic constants	[10]
C_{12}	133 GPa		
C_{44}	125 GPa		
μ_0	124 GPa	Shear modulus $(1/5)(C_{11}-C_{12})+(3/5)C_{44}$	Voigt average
B_0	214 GPa	Isothermal bulk modulus $(1/3)(C_{11}+2C_{12})$	
B_{T0}	216 GPa	Isentropic bulk modulus	Eq. (6)
$\partial\mu/\partial p$	0.95	Pressure derivative of shear modulus	[13]
$\partial B/\partial p$	4.2	Pressure derivative of bulk modulus	[13]
$\partial\mu/\partial\theta$	-0.012 GPa/K	Temperature derivative of shear modulus	[13]
$\partial B/\partial\theta$	-0.017 GPa/K	Temperature derivative of bulk modulus	[13]

Table 4 Theoretical dislocation properties

Plane	Burgers	b (Å)	d (Å)	Line and type ^a	\hat{K} (GPa)	$\hat{\mu}$ (GPa) ^b	W (eV/Å) ^c	τ_{PN} (GPa)
{111}	1/2[110]	5.62	4.59	[110] screw	123	124	24.4	1.49
				[101] mixed	156		30.1	0.49
				Isotropic edge	167		32.9	0.34
	1/4[110]	2.81	4.59	[110] screw	123		6.1	-
				[101] mixed	156		7.7	-
				Isotropic edge	167		8.2	-
{110}	1/2[110]	5.62	5.62	[110] screw	123	122	24.4	0.43
				Isotropic edge	167		32.9	6.2×10^{-2}
	1/4[110]	2.81	5.62	[110] screw	123		6.1	-
				Isotropic edge	167		8.2	-
{100}	1/2[110]	5.62	7.95	[110] screw	123	125	24.4	3.8×10^{-2}
				Isotropic edge	167		32.9	2.4×10^{-3}
	1/4[110]	2.81	7.95	[110] screw	123		6.1	-
				Isotropic edge	167		8.2	-

^aAnisotropic solutions for screw and mixed only; isotropic solutions for edge valid for any line direction.

^bFormulae listed in Appendix.

^cAssuming $\log(R/R_0)=4\pi$.

Table 5 Theoretical shear fracture and twinning properties

Plane	Burgers	b (Å)	d (Å)	$\hat{\mu}$ (GPa)	τ_F (GPa)	$\bar{\gamma}$ (J/m ²)	τ_T (GPa)
{111}	1/2[110]	5.62	4.59	124	24.2	-	-
	1/12[112]	1.62	-	-	-	0.104 ^a	0.64
	1/12[112]	1.62	-	-	-	0.140 ^b	0.86
{110}	1/2[110]	5.62	5.62	122	19.4	-	-
{100}	1/2[110]	5.62	7.95	125	14.1	-	-

^aScrew dislocation.^bEdge dislocation.

sistance to slip on {111} planes than on {110} or {100} [8]. Experiments of Veyssiere et al. [8] involved the compression of single crystals under confining pressure. In contrast, studies of Knoop (indentation) microhardness profiles of MgO–Al₂O₃ and MgO–3Al₂O₃ spinel single crystals [36] suggest that <110>{111} are active slip systems at room temperature although such experiments suggest secondary slip on <110>{110} could be possible in the latter (nonstoichiometric) spinel. In recovered samples of shock-loaded polycrystalline MgO–Al₂O₃, full 1/2{110}<111> dislocations and {111} twin lamellae have been observed via transmission electron microscopy [37]. For completeness, slip on {100} is also addressed in Table 4 since {110}<100> slip has been observed in spinel crystals, albeit with higher room temperature resistance than {110}<110> slip [8]. From Table 4, analytical Peierls–Nabarro stresses are greater for slip on {111} planes than for slip on {110} planes, in qualitative agreement with trends reported for MgO–*n*Al₂O₃ spinel (*n* ~ 1.1) [8]. However, the Peierls–Nabarro stress for slip on {100} is much lower than that for slip on {111}, in disagreement with experimental shear strengths reported for other spinels [8,36]. Dislocation core energies often obtained via atomic calculations are presently unknown for AlON and are not addressed in Table 4. Properties pertaining to twinning and shear fracture are listed in Table 5. Twinning stress and theoretical shear fracture strength are estimated, respectively, as [2,17,23]

$$\tau_T = \bar{\gamma}/b, \quad \tau_F = \hat{\mu}b/(2\pi d) \quad (14)$$

where b in the first of Eq. (14) is the magnitude of the Burgers vector of the partial dislocation associated with twinning and b in the second of Eq. (14) is the magnitude of a full Burgers vector on the cleavage plane. Twinning is considered to occur on {111} planes with corresponding partial Burgers vector 1/12[112] [38]. Stacking fault energy $\bar{\gamma}$ is estimated with an isotropic linear elastic approximation [9]:

$$\bar{\gamma} = \mu b^2/(2\pi R_{eq})[\cos^2 \phi + \sin^2 \phi/(1 - \nu)] \quad (15)$$

where ϕ is the angle between the Burgers vector and dislocation line, the equilibrium spacing R_{eq} between partial dislocations is 15 nm [4], and $\nu = (3B - 2\mu)/(6B + 2\mu)$ is the Poisson's ratio. Computed {111} stacking fault energy of AlON in Table 5 is comparable to that observed for MgAl₂O₄ spinel [9]. Properties in Tables 4 and 5 serve as guidance for continuum model parameters pertaining to defects entering Eqs. (4) and (11), as discussed in Sec. 4. Peierls–Nabarro stresses have been used elsewhere to explain plastic slip resistance in ceramic single crystals [1,2] and theoretical strengths have been considered elsewhere for use as failure criteria for other ceramics subjected to impact loading [2,20].

4 Model Application: High-Pressure Loading of Aluminum Oxynitride

The model outlined in Sec. 2 is applied to AlON [39] single- and polycrystals deformed under high-pressure loading as occurring in plate impact experiments [12,24–27]. Because data for the impact response of individual single crystals are not available, polycrystalline data are used to guide selection of certain model param-

eters for slip, twinning, pore collapse, and shear fracture. For instances wherein sufficient data are not available to enable unique parameter selection (e.g., initial resistances for slip and twinning on various families of crystallographic planes), several parameter sets are explored.

4.1 Slip and Twinning Parameters. The following relationships are used for slip and twin resistances entering flow rules in Eq. (11):

$$\tau_C^i = (\tau_{C0}^i + \Delta\tau_C^i)(\mu/\mu_0), \quad \tau_C^j = (\tau_{C0}^j + \Delta\tau_C^j)(\mu/\mu_0) \quad (16)$$

$$\Delta\tau_C^i = h \left(\sum_i \dot{\gamma}^i + \sum_j \dot{\gamma}^j \right), \quad \Delta\tau_C^j = h \left(\sum_i \dot{\gamma}^i + \sum_j \dot{\gamma}^j \right) \quad (17)$$

In Eq. (16), τ_{C0}^i and τ_{C0}^j are the constant initial values of slip and twin resistances that may differ among families of slip and twin systems, $\Delta\tau_C^i$ and $\Delta\tau_C^j$ account for the changes in slip and twinning resistance with the changes in defect densities at standard temperature and pressure, μ_0 is the shear modulus at standard temperature and pressure (the constant Voigt average in Table 3), and μ is the effective shear modulus that depends, like bulk modulus B , linearly on temperature and pressure

$$\mu = \mu_0 + p(\partial\mu/\partial p) + (\theta - \theta_0)(\partial\mu/\partial\theta), \quad B = B_0 + p(\partial B/\partial p) + (\theta - \theta_0)(\partial B/\partial\theta) \quad (18)$$

In the first of Eq. (16), scaling of the slip resistance by μ/μ_0 follows the assertion that slip resistance should be proportional to the instantaneous shear modulus [40,41] and results in relatively mild influences of pressure and temperature on yield strength. The variation of yield stress with temperature could conceivably be more substantial, e.g., represented by Arrhenius-type kinetics or temperature-dependent dislocation drag, but sufficient data are not available for AlON to justify a more complicated relation. Twinning resistance follows an analogous prescription in the second of Eq. (16). In Eq. (17), h is a constant hardening modulus and all slip and twin systems harden at the same rate, the simplest realistic assumption possible (i.e., equal self- and latent-hardening). The model in Eq. (17) represents the following general physics [17,42]: Accumulated dislocations and twin boundaries act as barriers to slip and further twinning. The relationship between accumulated dislocation density and change in slip resistance is assumed to follow the usual Taylor-type law [2,43–45] deemed applicable for spinel ceramics [9]:

$$\Delta\tau_C^i = \alpha\mu b\sqrt{\rho_D} \quad (19)$$

where α for most materials lies between 0.1 and 1.0 [9]. The area per unit volume of twin boundaries obtained from simple geometric considerations is

$$\eta_T = 2 \sum_j \dot{\gamma}^j / t_T = 2f_T / t_T \quad (20)$$

with t_T as the thickness of twin lamellae characteristic of twin structures observed in AlON deformed at high rates [4,7].

Parameters entering the single crystal constitutive model are listed in Table 6. Hardening modulus h is chosen to simulta-

Table 6 Parameters for a single crystal plasticity model

Parameter	Value	Definition
h	1.0 GPa	Hardening modulus
$\dot{\gamma}_0$	1.0/s	Reference strain rate
m and n	10	Strain rate sensitivity
γ^j	$\sqrt{2}/2$	Twinning shear
b	5.62 Å	Burgers magnitude
\hat{K}	$123-0.012(\theta-\theta_0)$ GPa	Dislocation energy factor
$\bar{\gamma}$	0.14 J/m ²	Stacking fault energy
α	0.5	Proportionality constant
t_T	10 μm	Characteristic twin thickness

neously produce an accurate representation of the shear stress response of polycrystalline AION subjected to uniaxial strain loading and a physically reasonable dislocation density in Eq. (19), as discussed later in Sec. 4.2. Rate sensitivity parameters follow from experimental observations on alumina (α -Al₂O₃) [46]. Note that AION, stoichiometrically, is related to both alumina and aluminum nitride [7,11], so use of alumina data to justify selection of m may be a reasonable first assumption in the absence of test data for AION or spinel. In many crystalline solids, inverse rate sensitivity $1/m$ increases with loading rate; the value chosen here for impact loading ($1/m=0.1$) may not apply at lower strain rates. Coefficient $\dot{\gamma}_0$ provides dimensional consistency. Twinning shear γ^j is standard for a compound twin in spinel [38,47]. Representatively, b is taken as the full Burgers vector for $\langle 110 \rangle$ slip, \hat{K} is chosen as the anisotropic energy factor for a screw dislocation (Table 4) with a temperature dependence equal to that of the shear modulus (Table 3), stacking fault energy $\bar{\gamma}$ is that for a twinning edge partial (Table 5), α in Eq. (19) is assigned a typical value of 0.5, and the characteristic twin thickness is 10 μm [7] on the order of 1/10 of a typical grain diameter.

The following slip systems are incorporated in subsequent calculations: $\{111\}\langle 110 \rangle$, $\{110\}\langle 110 \rangle$, and $\{100\}\langle 110 \rangle$, all which have been observed in spinel ceramics [8,9]. Twinning systems are of type $\{111\}\langle 112 \rangle$ [38]. Four sets of values for initial hardness of slip/twin systems in Eq. (16) are explored, as listed in Table 7. The first of set assumes that all the slip and twinning resistances are equal, the simplest assumption incorporating all possible mechanisms. The second set assumes that the only significant inelastic deformation mode is $\{111\}\langle 110 \rangle$ slip, in agreement with indentation anisotropy profiles for MgO–Al₂O₃ spinel single crystals [36], which do not seem to twin readily [9] although $\{111\}$ twin lamellae have been observed in shock recovered specimens [37]. The third set assumes that a ratio of initial resistances for shear on $\{111\}$: $\{110\}$: $\{100\}$ planes of 2:1:2, motivated by experimental observations for MgO– n Al₂O₃ spinel ($n \sim 1.1$) [8] at or below 400°C. The fourth set assumes that the ratio of initial twinning resistance to initial slip resistance on all systems is 1:2. Initial resistances for slip are comparable to Peierls–Nabarro stresses for screw, mixed, or edge dislocations on $\{111\}$ and $\{110\}$ planes computed from Eq. (13) and listed in the rightmost column of

Table 4; initial resistances for twinning are comparable to theoretical estimates computed from Eq. (14) and listed in the rightmost column of Table 5.

Twinning induces a 180 deg reflection or rotation of the lattice vectors about the habit plane normal or about the twin axis [42,47]. For compound twins in centrosymmetric crystals, such an orthogonal transformation for twin system j can be represented by matrix $Q_{\alpha\beta}^j = 2m_{\alpha}^j m_{\beta}^j - \delta_{\alpha\beta}$, a 180 deg rotation about habit plane unit normal m_{α}^j . Re-orientation of the elastic modulus tensor due to twinning [2] is not required in the present study because of the low elastic anisotropy of AION (Zener's ratio $2C_{44}/(C_{11}-C_{12}) = 1.02 \approx 1$) and lattice orientation does not affect the thermal expansion coefficient for a cubic crystal. Twinning is unidirectional in Eq. (11); when the resolved shear stress is negative on the habit plane in the direction of positive shear, inelastic deformation on $\{111\}$ planes can result only from glide of partial dislocations. In a previous model [2], the summed contribution from slip rates in the first of Eq. (3) was weighted by factor $1-f_T$ and new secondary slip systems could become active within the twins. In the present model, factor $1-f_T$ is omitted but an offsetting resistance to slip is reflected by hardening due to twinning in Eq. (17). For simplicity and because of insufficient microscopy data for AION to justify a more complicated theory, new slip systems are not activated within twins in the present application and successive twins of a different orientation within a given twin (including reversal or detwinning) are not modeled explicitly. In calculations that follow, the volume fraction of twins in any crystal always remains less than 20% (preferred $\{111\}$ twinning in Table 7) and usually remains less than 5% (all other cases in Table 7). This model might be inappropriate for conditions wherein the total twin volume fraction approaches unity.

4.2 Polycrystal Modeling. The porosity of a polycrystal can significantly affect its mechanical response. To first address the effect of porosity independently from slip or twinning, the response of an aggregate of grains subject to hydrostatic pressure is studied. For a cubic crystal, the deviatoric and volumetric stress-strain responses are decoupled and the stress in a cubic crystal subject to spherical compression is hydrostatic pressure, independent of the crystal's lattice orientation. For a prescribed change in volume, the average pressure \bar{p} supported by a polycrystal depends on the aggregate's effective bulk modulus, porosity, and temperature. The influence of porosity on effective bulk modulus \bar{B} and effective shear modulus $\bar{\mu}$ of the polycrystalline aggregate is represented here using the self-consistent model of Mackenzie [48]

$$\bar{B} = 4\mu B(1 - \vartheta)/[4\mu + 3B\vartheta], \quad \bar{\mu} = \mu[1 - 5\vartheta(3B + 4\mu)/(9B + 8\mu)] \quad (21)$$

where ϑ is the porosity and μ and B are the effective shear and bulk moduli of the fully dense crystal that depend on pressure and temperature, as in Eq. (18). Above a threshold pressure, pores may collapse irreversibly. This phenomenon, common in brittle ceramics, minerals, and geologic materials [18,22], is modeled via [19]

Table 7 Initial resistances for slip and twin systems in a crystal plasticity model

Slip or twin system	τ_{c0} all systems equal (GPa)	τ_{c0} exclusive $\{111\}$ slip (GPa)	τ_{c0} preferred $\{110\}$ slip (GPa)	τ_{c0} preferred $\{111\}$ twinning (GPa)
$\{111\}\langle 110 \rangle$ slip	1.00	0.75	1.10	1.50
$\{110\}\langle 110 \rangle$ slip	1.00	∞	0.55	1.50
$\{100\}\langle 110 \rangle$ slip	1.00	∞	1.10	1.50
$\{111\}\langle 112 \rangle$ twin	1.00	∞	1.10	0.75

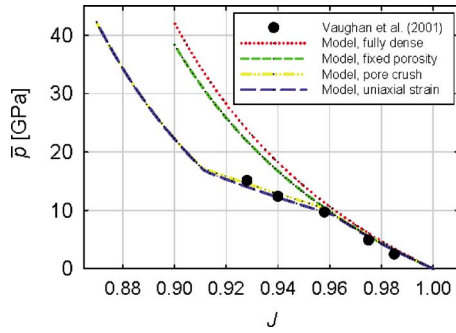


Fig. 1 Hydrostatic pressure for polycrystalline AION: experiments [25] and model predictions

$$\delta\vartheta = \begin{cases} R\delta\bar{p}[H(\bar{p} - p_0)H(\delta\bar{p})] & [\vartheta > 0] \\ 0 & [\vartheta = 0] \end{cases} \quad (22)$$

where $\delta\vartheta$ is an incremental reduction in porosity commensurate with average pressure increase $\delta\bar{p}$ supported by the aggregate, R is a negative constant dictating the rate of pore collapse, $H(\cdot)$ is a Heaviside's step function, and p_0 is a threshold pressure.

Model results are shown in Fig. 1 for AION subjected to spherical compression. Experimental data are from impact experiments [25] reproduced in Ref. [12]. In the application of the model corresponding to Fig. 1, adiabatic conditions are assumed and thermoelastic heating is taken into account (fifth term on the right in Eq. (9)) but no slip or twinning occurs because no shear stresses are generated during spherical compression. The average pressure is \bar{p} and the total volume change of the aggregate (crystals and pores) is measured by Jacobian

$$J = J^E[1 - (\vartheta_0 - \vartheta)] \quad (23)$$

where ϑ_0 is the initial porosity and J^E is the elastic compression that is identical in each grain. Four model curves are shown with the test data. The most accurate fit is provided by the curve labeled "pore crush," which uses Eqs. (21) and (22), with parameters for Eq. (22) listed in Table 8. Initial porosity ϑ_0 is consistent with the initial mass density of specimens used in experiments [25]. The curve labeled "fully dense" corresponds to predictions for a crystal with null porosity. The curve labeled "fixed porosity" assumes no pore collapse ($R=0$ in Eq. (22)) but allows for a reduction in bulk modulus via a fixed value of ϑ_0 in Eq. (21). Also shown is a curve for uniaxial strain loading conditions that will be discussed later; this "uniaxial strain" curve is obtained using Eqs. (21) and (22) and is nearly identical to the response for spherical compression. The regime, where the slope of pressure versus volume is reduced, corresponds to contributions from collapsing pores. From Fig. 1, when pore collapse is omitted, average pressure is severely overestimated for compression greater than 4% (i.e., for $J < 0.96$).

Considered next is the response of an aggregate of N randomly oriented crystals of equal volume subjected to uniaxial strain. The aggregate also contains initial porosity ϑ_0 , which can be concentrated at boundaries between grains. Results that follow for poly-

crystals follow the Taylor assumption [44,49,50]: All grains in the aggregate are subject to same deformation gradient components F_{aA} . This assumption is deemed more appropriate than other simple averaging schemes (e.g., those that assume constant stress in all grains) for highly confined loading conditions [50]. For uniaxial strain, the deformation gradient in matrix form is

$$[F] = \begin{bmatrix} 1 - \dot{\epsilon}t & 0 & 0 \\ 0 & 1 & 0 \\ 0 & 0 & 1 \end{bmatrix} \quad (24)$$

where $\dot{\epsilon}$ is the applied strain rate positive for compression. The rate used in all calculations that follow is $\dot{\epsilon} = 10^5/\text{s}$, representative of plate impact [21]. For the present set of boundary conditions, elastic volume change J^E is identical in each grain and Eq. (23) again describes the total volume change of the porous aggregate. Deviatoric elastic and plastic deformations differ among grains with different initial orientations. Average and local deviatoric Cauchy stress components are defined, respectively, as

$$\bar{\sigma}'_{ab} = \frac{1}{N} \sum_N \sigma'_{ab}, \quad \sigma'_{ab} = \sigma_{ab} + p\delta_{ab} \quad (25)$$

with $\bar{\mu}$ computed from Eq. (21) using the porosity, the average temperature, and the average pressure in the grains to determine elastic coefficients of the matrix in Eq. (18). Average temperature, twin volume fraction, and dislocation density in the grains are

$$\bar{\theta} = (1/N) \sum_N \theta, \quad \bar{f}_T = (1/N) \sum_N f_T, \quad \text{and} \quad \bar{\rho}_D = (1/N) \sum_N \rho_D \quad (26)$$

The average pressure for the porous polycrystalline aggregate is

$$\bar{p} = \frac{1}{N\bar{B}} \sum_N p \quad (27)$$

where \bar{B} is computed from Eq. (21). The maximum shear stress for the aggregate is defined as

$$\bar{\tau} = (\bar{\sigma}'_{\max} - \bar{\sigma}'_{\min})/2 \quad (28)$$

where $\bar{\sigma}'_{\max}$ and $\bar{\sigma}'_{\min}$ are the maximum and minimum principle values of the first of Eq. (25). Under confined uniaxial strain compression Eq. (24), the present material (consisting of cubic crystals and pores) experiences no tensile stress. However, above some threshold maximum shear stress $\bar{\tau}_F$, the material may fail due to cleavage or grain boundary fracture. After such failure occurs, the material consists of numerous fragmented grains and is represented as an isotropic, compressible, and viscous medium. Considered in some calculations that follow is a shear failure model that takes effect for $\bar{\tau} \geq \bar{\tau}_F$, providing the following relations for average deviatoric stress and temperature rise in the post-fracture regime:

$$\bar{\sigma}'_{ab} = 2\chi D'_{ab}, \quad \dot{\bar{\theta}} = J^E \bar{\sigma}'_{ab} D'_{ab} / (\rho_0 c_V) \quad (29)$$

The deviatoric deformation rate is $D'_{ab} = (L_{ab} + L_{ba})/2 - \delta_{ab} L_{cc}/3$. The post-fracture dynamic viscosity is χ and is assumed constant for simplicity in Table 8 although a more general treatment would permit possible dependence of sliding friction of fragmented grains on pressure and, perhaps, temperature and loading rate [22]. For $\bar{\tau} \geq \bar{\tau}_F$, pressure is computed in same way as in Eq. (27). The second of Eq. (29) represents the temperature rise from dissipation due to shear friction of fractured grains sliding past one another. Numerical algorithms for the present thermoelastic-plastic calculations extend those used in previous work for large, high-rate deformations of cubic crystals [31,44,45] to account for aforementioned slip, twinning, pore collapse, and shear fracture mechanisms thought relevant for AION

Table 8 Parameters for polycrystal pore collapse and shear fracture models

Parameter	Value	Definition
ϑ_0	0.033	Initial porosity
p_0	10.0 GPa	Initiation pressure for pore collapse
R	-0.005/GPa	Pore collapse coefficient
$\bar{\tau}_F$	3.5 GPa	Macroscopic shear fracture strength
χ	3.25×10^{-5} GPa-s	Post-fracture dynamic viscosity

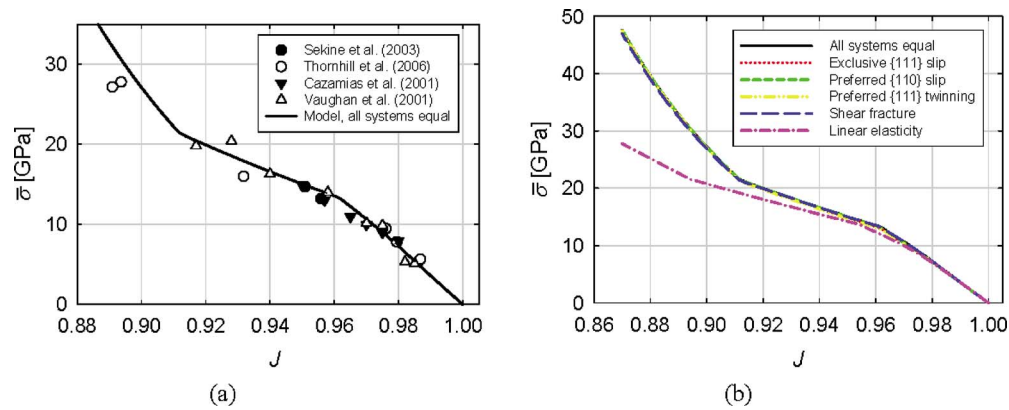


Fig. 2 Axial stress for polycrystalline AlON in uniaxial strain: (a) experiments [24–27] and model predictions (equal slip and twin resistances) and (b) model predictions for various slip/twin/fracture parameters and elasticity models (upper four curves in (b) are nearly indistinguishable)

polycrystals.

Stress-strain data and model predictions are shown in Fig. 2. Axial stress supported by the aggregate is

$$\bar{\sigma} = -(\bar{\sigma}'_{11} - \bar{p}) \quad (30)$$

positive in compression. Predictions shown in Fig. 2(a) assume that all slip/twin systems have equal hardness (column 2 of Table 7). Predictions in Fig. 2(b) account for the four sets of initial slip/twin system hardness values listed in columns of Table 7 and for the shear fracture model of Eq. (29). Predictions for the latter (shear fracture) model also assume equal hardness among slip/twin systems for $\bar{\tau} < \bar{\tau}_f$. Also shown in Fig. 2(b) are results labeled “linear elasticity,” which are obtained using the same model parameters as “all systems equal” with the exception that pressure- and temperature-derivatives of elastic moduli are set to zero. All model results that incorporate nonlinear elasticity are nearly indistinguishable in Fig. 2(b) and thus provide an accurate fit to the plate impact data [24–27] in Fig. 2(a). Model results incorporating linear elasticity noticeably underpredict the axial stress for large compressions, i.e., for $J < 0.97$. Notice that pores are crushed according to Eq. (22); their contribution to volume change, deviatoric stress, and pressure is incorporated in Eqs. (23), (25), and (27), respectively. It was determined that $N=100$ (i.e., 100 random grain orientations) was sufficient to ensure a macroscopically isotropic response insensitive to further increases in N .

Shear stresses supported by the aggregate are shown in Fig. 3; predictions are computed via Eq. (28). All predictions in Fig. 3 provide a reasonable description of the experimental data [12,25], which exhibit notable scatter. As summarized elsewhere [12], ex-

periments by other researchers have indicated that the shear strength of AlON polycrystals shocked above the Hugoniot elastic limit (HEL) typically falls in the range 3.3–3.9 GPa, in general agreement with model predictions in Fig. 3. The experimental HEL corresponds to $\bar{\sigma} \approx 10$ –12 GPa or $J \approx 0.97$ [12,26,27]. Initial resistances to slip or twinning used in the model (Table 7) are ~ 1 GPa, of the order of Peierls–Nabarro stresses for {111} and {110} slip of screw dislocations (Table 4) and comparable to shear strengths for slip in other spinel crystals (~ 1 –2 GPa) [8] but are an order of magnitude smaller than theoretical strengths predicted for AlON (Table 5). At larger compressive strains, predicted shear stresses will continue to increase for all cases except the model incorporating shear fracture for which shear stress increases little for $J < 0.93$. Plate impact experiments on AlON have demonstrated a reduction in spall strength from 1.7 GPa to 0.14 GPa as the impact stress is increased from 4.8 GPa to 9.5 GPa [24,27], indicating that some local shear-induced damage or fracture processes may take place at impact pressures below 9.5 GPa. It is thus likely that a model incorporating shear fracture (e.g., via Eq. (29)) is physically realistic for AlON polycrystals subject to impact stresses on the order of the HEL. Hardening law for slip Eq. (17) could be modified so that strain hardening ceases above some saturation stress [29,44,45]; however, from the preceding arguments, it may be reasonable to assume that during monotonic impact loading, hardening and accumulation of dislocations by Eq. (19) and twin boundaries by Eq. (20) proceed until fracture. Intragranular fracture may be initiated as a result of local stress concentrations due to interactions of dislocations and twin boundaries [42].

Predictions for average temperature rise during adiabatic uniaxial straining of the aggregate are shown in Fig. 4, wherein

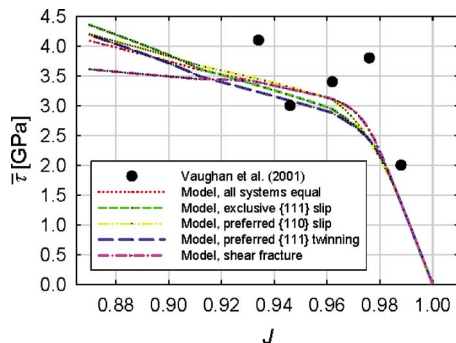


Fig. 3 Maximum shear stress for polycrystalline AlON in uniaxial strain: experiments [25] and predictions for slip/twin/fracture model parameters

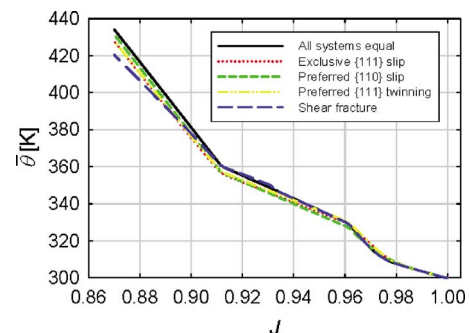


Fig. 4 Average temperature for polycrystalline AlON in uniaxial strain: model predictions

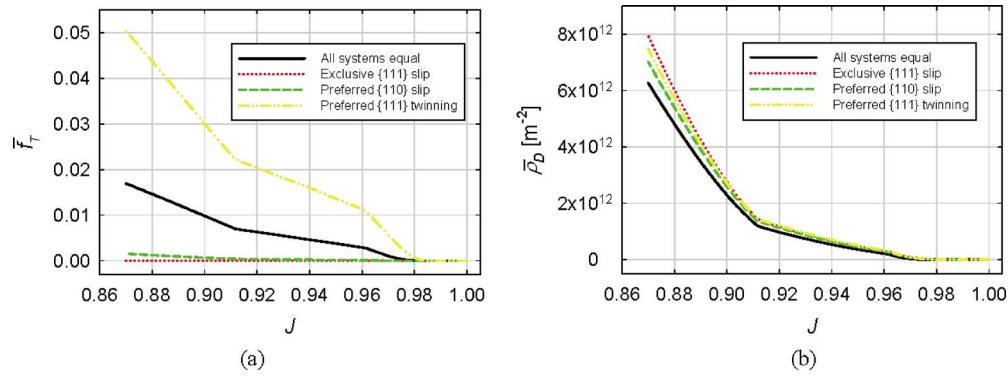


Fig. 5 Predicted defect densities for polycrystalline AlON in uniaxial strain: (a) total twin volume fraction and (b) dislocation density

the local temperature of each grain is updated according to Eq. (9) with $r=0$ and $\nabla^2\theta=0$. The different initial slip/twin hardness values and the use of shear fracture model all result in similar average temperature predictions. In hydrostatic compression calculations corresponding to Fig. 1, the temperature rise resulting from thermoelasticity alone (fifth term on the right of Eq. (9)) is ~ 20 K at $J=0.87$. For uniaxial strain corresponding to Fig. 4 at $J=0.87$, the adiabatic temperature rise resulting from plastic dissipation less the energy storage associated with lattice defects associated with the rightmost two terms in Eq. (9) is ~ 100 K. Possible temperature rise in the material associated explicitly with pore collapse (e.g., adiabatic heating in highly plastically deformed regions surrounding voids and heat transfer between crystals and compressed gas/vapor within voids) is omitted in the present analysis, as is that resulting from any additional local dissipation associated with passage of a shock front.

Predicted twin volume fractions are shown in Fig. 5(a). When the critical shear stress required for twinning is reduced, as dem-

onstrated in results for “preferred {111} twinning,” the volume fraction of twins produced during the deformation process increases. When {110} slip is favored, on the other hand, the fraction of twins produced decreases relative to results in which all slip and twin systems have equal strength. During all calculations, the maximum volume fraction of twins in any grain always remained less than 0.2. For calculations incorporating exclusive {111} slip, twinning is prohibited so the volume fraction of twins for that case is zero. The present results suggest that experimental measurements of twin volume fractions in recovered samples should provide insight into possible preference of slip or twinning in AlON deformed at high rates under confining pressure. Figure 5(b) shows predicted dislocation densities. Magnitudes are comparable to those observed for other spinel crystals undergoing plastic deformation [9]. Experimental and theoretical studies have suggested that local residual stress fields of dislocations may impart a (small) volume change in crystals, which can be estimated as [2,31,32]

$$\delta V/l = \begin{cases} \frac{1}{3} \left[\frac{1-\nu-2\nu^2}{(1-\nu)B} \left(\frac{\partial B}{\partial p} - 1 \right) + \frac{2-2\nu+2\nu^2}{(1-\nu)\mu} \left(\frac{\partial \mu}{\partial p} - \frac{\mu}{B} \right) \right] W & \text{(edge dislocations)} \\ \frac{1}{\mu} \left(\frac{\partial \mu}{\partial p} - \frac{\mu}{B} \right) W & \text{(screw dislocations)} \end{cases} \quad (31)$$

where $\delta V/l$ is the volume change per unit length of dislocation line and W is the energy per unit length (Table 4). From Eq. (31) and Tables 3 and 4, $\delta V/l = 3.3 \times 10^{-19}$ m² for $1/2\langle 110 \rangle$ edge dislocations and $\delta V/l = 1.2 \times 10^{-19}$ m² for $1/2\langle 110 \rangle$ screw dislocations, predictions comparable to those for other ceramics [2,23]. For a dislocation density of $\rho_D = 10^{13}$ m⁻², the volumetric strain associated with such (edge) dislocations is $\rho_D \times \delta V/l = 3.3 \times 10^{-6}$, negligible in comparison to applied volumetric strains on the order of 0.01. Thus, omission of volume changes associated with dislocations, as indicated in Eqs. (1)–(3), is a reasonable modeling assumption for the present loading conditions.

4.3 Single Crystal Predictions. Investigated next are responses of single crystals of several orientations subjected to uniaxial strain Eq. (24) at a fixed rate of $\dot{\epsilon} = 10^5$ /s and again assuming adiabatic conditions. Crystals are treated in Sec. 4.3 as fully dense (i.e., null porosity) and failure associated with fracture at grain boundaries addressed via Eq. (29) for polycrystals is not considered for single crystals. Two initial lattice orientations are considered. The first, labeled [100], corresponds to the alignment

of the crystal’s cube axes with the global coordinate system, so that compression in Eq. (24) is normal to the (100) plane. The second orientation, labeled [110], corresponds to Goss orientation of texture analysis [51] with Bunge’s Euler angles ($\varphi_1 = 0$ deg, $\Phi = 45$ deg, and $\varphi_2 = 90$ deg), so that compression in Eq. (24) is normal to the (110) plane. The four sets of initial slip/twin system resistances listed in Table 7 are investigated for each orientation. For comparison purposes, also considered in what follows are predictions for a fully dense polycrystal ($N=100$) assuming equal slip/twin resistances.

Axial stresses are shown in Fig. 6(a). Because hydrostatic pressures are nearly identical for each orientation and for each choice of slip/twin resistance and because hydrostatic pressures are relatively large compared with deviatoric stress components, differences in axial stresses among various cases are small, at most $\sim 5\%$. Maximum shear stresses computed from Eq. (28) are shown in Fig. 6(b). Significant differences in predicted shear stresses among orientations and among choices of initial slip/twin strengths are evident. Average shear stresses supported by the polycrystal fall about midway between those for the stiffest and

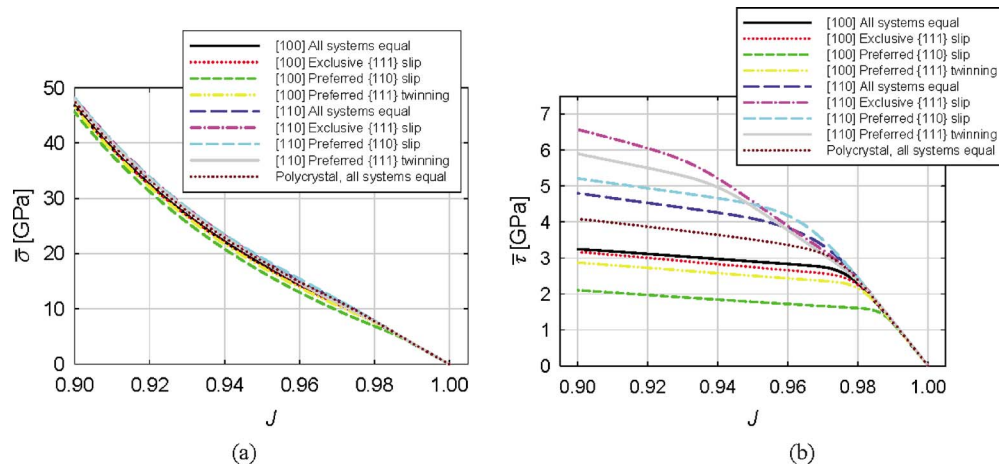


Fig. 6 Predicted (a) axial stress and (b) maximum shear stress for AlON in uniaxial strain: single crystals (various slip/twin models) and a fully dense polycrystal

most compliant single crystals considered in Fig. 6(b). For single crystals of the [110] orientation, lateral stress $\sigma_{22} \neq \sigma_{33}$. The reduction in slope associated with pore crushing evident in Fig. 2 (over range $0.96 > J > 0.91$) is absent for the fully dense crystals considered in Fig. 6(a).

Figure 7(a) shows the predicted twin volume fractions. Clearly, evolution of twin fractions depends strongly on initial lattice orientation and relative hardness of slip/twin systems. For the single crystal oriented at [100] with {111} twinning preferred, the twin volume fraction approaches 15% at $J=0.9$ (i.e., at 10% compressive strain). For a single crystal with the same set of slip/twin resistances compressed along [110], the twin volume fraction ap-

proaches only 3% at $J=0.9$. Several other cases including single crystals with preferred {110} slip demonstrate almost no twinning (recall also that twinning is prohibited for exclusive {111} slip). Predicted dislocation densities are shown in Fig. 7(b). Over most of the compression range, the [100] orientation with preferred slip on {110} or {111} planes produce the largest dislocation density while the polycrystal produces the lowest.

Table 9 lists for $J=0.97$ and $J=0.9$ (3% and 10% compressions, respectively), the ratio of maximum shear stress on each of the cleavage planes to its corresponding theoretical shear strength given in Table 5. Substantial differences are evident among crystal orientations and initial slip/twin resistances used in the model. For

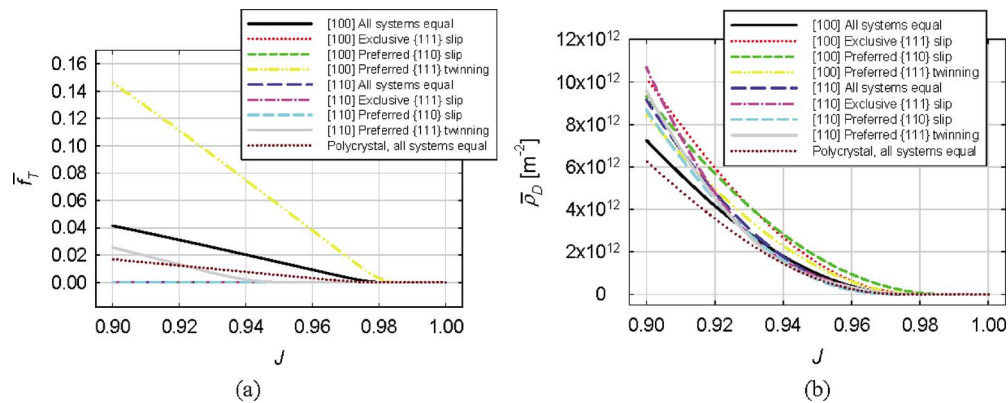


Fig. 7 Predicted total twin volume fraction (curve not visible \$\leftrightarrow\$ negligible values) (a) and dislocation density (b) for AlON in uniaxial strain: single crystals (various slip/twin models) and a fully dense polycrystal

Table 9 Ratio of maximum shear stress to theoretical strengths at 3% and 10% uniaxial compressions

Crystal orientation and slip/twin hardness model	$\tau_{\max} / \tau_F \{111\}$		$\tau_{\max} / \tau_F \{110\}$		$\tau_{\max} / \tau_F \{100\}$	
	$J=0.97$	$J=0.90$	$J=0.97$	$J=0.90$	$J=0.97$	$J=0.90$
[100] all systems equal	0.106	0.119	0.139	0.157	0	0
[100] exclusive {111} slip	0.099	0.116	0.130	0.153	0	0
[100] preferred {110} slip	0.063	0.077	0.084	0.102	0	0
[100] preferred {111} twinning	0.091	0.105	0.120	0.139	0	0
[110] all systems equal	0.116	0.131	0.140	0.175	0.234	0.319
[110] exclusive {111} slip	0.102	0.125	0.128	0.224	0.224	0.435
[110] preferred {110} slip	0.119	0.142	0.145	0.191	0.245	0.346
[110] preferred {111} twinning	0.093	0.113	0.121	0.201	0.217	0.390

grains of the [100] orientation, shear stresses on {100} planes vanish identically. Recovered fragments from dynamic experiments on AlON polycrystals suggest that intragranular fracture occurs on {111} planes [4]. At $J=0.9$, the maximum shear stress on any {111} plane obtained among any considered set of orientations and initial slip/twin resistances is $\sim 14\%$ of the theoretical strength. Results in Table 9 suggest that fracture might occur first on {100} planes for crystals of [110] orientation if the theoretical shear strength computed via the second of Eq. (14) is realistic. However, in the present context, Eq. (14) should be regarded only as an order of magnitude approximation since it depends only on the appropriate shear elastic constant and interplanar spacing and does not account for details of atomic bonding (e.g., local charge imbalances across fracture planes) in spinel ceramics such as AlON. The experimentally measured fracture toughness for MgAl_2O_4 spinel single crystals is lowest on {100} planes [52], often quoted as the primary observed (tensile) cleavage planes for that material; however, atomic modeling [53] has suggested that {111} planes in spinel ceramics should be of the lowest surface energy and cleavage may be preferred on these planes. At $J=0.97$, the approximate compressive strain in an AlON polycrystal at its HEL, the ratio of maximum shear stress to theoretical strength on any of the planes considered in Table 9 is substantial (i.e., $\sim 25\%$), supporting the notion that transgranular fracture of grains can take place during high rate compression [7,26].

5 Conclusions

A model has been developed for nonlinear mechanics of elastic-plastic ceramic crystals with the spinel structure. Nonlinear elasticity, anisotropy, thermal expansion, dislocation glide, twinning, shear fracture, and pore collapse are addressed for AlON crystals in what appears to be the first documented study of AlON using large deformation crystal plasticity theory. A number of physically relevant material properties corresponding to thermomechanical behavior and lattice defects in AlON have been compiled or computed. Model calculations demonstrate an accurate depiction of pressures and shear stresses observed experimentally in shock-loaded polycrystals. Key findings regarding behaviors of AlON polycrystals and single crystals are summarized as follows:

- Hydrostatic pressures and axial stresses are predicted accurately (the latter to at least ~ 30 GPa) when nonlinear elasticity (i.e., pressure- and temperature-dependent moduli) and pore collapse are incorporated in the present model. Pressure is overestimated when pore collapse is omitted in the model and axial stress is underestimated when linear elasticity is used.
- Because of the large number of potential slip and twinning mechanisms in spinel crystals: slip on {111}, {110}, and {100} planes and twinning on {111} planes, available polycrystal test data are insufficient to enable a unique determination of shear strengths for all inelastic deformation modes. Several realistic sets of initial shear resistances have been investigated, as has a model for shear-induced fracture during impact loading; all results provide a reasonable description of macroscopic axial- and shear stress data.
- Initial resistances to continuum slip appear comparable to Peierls–Nabarro stresses computed via anisotropic elasticity for screw dislocations on {111} and {110} planes in the rate-independent limit. Initial resistance to twinning on {111} planes appears comparable to the ratio of stacking fault energy to the magnitude of the partial Burgers vector associated with twinning.
- Predictions for single crystals provide estimates of effects of lattice orientation on the response to loading representative of plate impact. Maximum shear stresses attained are highly sensitive to crystallographic orientation and to initial hardness ratios among families of slip and twin systems.
- Predicted twin volume fractions and cleavage fracture ten-

dencies vary strongly with grain orientation and initial resistance to slip or twinning. At applied strains corresponding to the polycrystalline HEL, maximum resolved shear stresses on low-index planes can approach 25% of the theoretical strength.

- Results point to the need for experimental measurements, either in situ (since AlON is transparent) or on recovered samples, of twin volume fractions to quantify preference, or lack thereof, for twinning versus slip at high rates of loading.

The content of the present paper has focused on constitutive model development and predictive calculations for AlON single crystals and polycrystals. Behavior in the latter has been described via a self-consistent assumption to account for effects of porosity (Eq. (21)) and a Taylor assumption for deformation of crystals comprising the matrix (Eq. (24)). A more refined approach, eliminating the above assumptions, would fully account for variations in local deformation among and within individual grains in a polycrystal as well as possible variations in behavior of individual pores and fracture planes in the microstructure. Finite element calculations, whereby individual grains and grain boundaries are resolved explicitly, [15,44,45] are presently in progress; results will be reported in future work.

Acknowledgment

I. Batyrev (ARL) is thanked for providing access to quantum mechanical predictions of elastic constants of AlON single crystals. Informative interactions with D. Dandekar (ARL), G. Gazonas (ARL), and J. McCauley (ARL) regarding physical properties and behaviors of ceramics are acknowledged.

Appendix

Expressions for shear elastic constant $\hat{\mu}$ used in expressions for anisotropic Peierls–Nabarro stress and theoretical strength in Eqs. (13) and (14) and Tables 4 and 5 are listed in what follows. In a coordinate system with axes aligned along the cubic axes, the three independent second-order elastic constants are C_{11} , C_{12} , and C_{44} . Components of the second-order compliance tensor are [54]

$$s_{11} = (C_{11} + C_{12}) / [(C_{11} - C_{12})(C_{11} + 2C_{12})],$$

$$s_{12} = -C_{12} / [(C_{11} - C_{12})(C_{11} + 2C_{12})], \quad \text{and} \quad s_{44} = 1/C_{44} \quad (\text{A1})$$

For shearing in a $\langle 110 \rangle$ direction on a {111} plane, the appropriate shear modulus is [55]

$$\hat{\mu} = 1 / \{2[s_{44} + (s_{11} - s_{12} - 2s_{44})/3]\} \quad (\text{A2})$$

For shearing in a $\langle 110 \rangle$ direction on a {110} plane, the appropriate shear modulus is [54,56]

$$\hat{\mu} = 1 / [2(s_{11} - s_{12})] = (C_{11} - C_{12}) / 2 \quad (\text{A3})$$

For shearing in a $\langle 110 \rangle$ direction on a {100} plane, the appropriate shear modulus is [54,56]

$$\hat{\mu} = 1/s_{44} = C_{44} \quad (\text{A4})$$

References

- [1] Farber, Y. A., Yoon, S. Y., Lagerlof, K. P. D., and Heuer, A. H., 1993, "Microplasticity During High Temperature Indentation and the Peierls Potential of Sapphire ($\alpha\text{-Al}_2\text{O}_3$) Single Crystals," *Phys. Status Solidi A*, **137**, pp. 485–498.
- [2] Clayton, J. D., 2009, "A Continuum Description of Nonlinear Elasticity, Slip and Twinning, With Application to Sapphire," *Proc. R. Soc. London, Ser. A*, **465**, pp. 307–334.
- [3] Lankford, J., Predebon, W. W., Staehler, J., Subhash, G., Pletka, B., and Anderson, C., 1998, "The Role of Plasticity as a Limiting Factor in the Compressive Failure of High Strength Ceramics," *Mech. Mater.*, **29**, pp. 205–218.
- [4] Paliwal, B., Ramesh, K. T., McCauley, J. W., and Chen, M., 2008, "Dynamic Compressive Failure of AlON Under Controlled Planar Confinement," *J. Am. Ceram. Soc.*, **91**, pp. 3619–3629.

- [5] Tymiak, N., Chrobak, D., Gerberich, W., Warren, O., and Nowak, R., 2009, "Role of Competition Between Slip and Twinning in Nanoscale Deformation of Sapphire," *Phys. Rev. B*, **79**, p. 174116.
- [6] Sickafus, K. E., Wills, J. M., and Grimes, J. W., 1999, "Structure of Spinel," *J. Am. Ceram. Soc.*, **82**, pp. 3279–3292.
- [7] McCauley, J. W., Patel, P., Chen, M., Gilde, G., Strassburger, E., Paliwal, B., Ramesh, K. T., and Dandekar, D. P., 2009, "AION: A Brief History of Its Emergence and Evolution," *J. Eur. Ceram. Soc.*, **29**, pp. 223–236.
- [8] Veysiere, P., Kirby, S. H., and Rabier, J., 1980, "Plastic Deformation of $\text{MgO}:\text{nAl}_2\text{O}_3$ Spinel at Temperatures Below 1000°C ($0.5 T_m$)," *J. Phys.*, **41**, pp. 175–178.
- [9] Mitchell, T. E., 1999, "Dislocations and Mechanical Properties of $\text{MgO}-\text{Al}_2\text{O}_3$ Spinel Single Crystals," *J. Am. Ceram. Soc.*, **82**, pp. 3305–3316.
- [10] Batyrev, I. G., Rice, B. M., and McCauley, J. W., 2009, "First Principles Calculations of Nitrogen Atomic Position Effects on Elastic Properties of Aluminum Oxynitride (AION) Spinel, Materials Research Society Fall Meeting, Boston, MA, Nov. 30–Dec. 1, Paper No. LL5.3.
- [11] Corbin, N. D., 1989, "Aluminum Oxynitride Spinel: A Review," *J. Eur. Ceram. Soc.*, **5**, pp. 143–154.
- [12] Dandekar, D. P., Vaughan, B. A. M., and Proud, W. G., 2007, "Shear Strength of Aluminum Oxynitride," *Shock Compression of Condensed Matter*, M. Elert, M. D. Furnish, R. Chau, N. Holmes, and J. Nguyen, eds., American Institute of Physics, Melville, NY.
- [13] Graham, E. K., Munly, W. C., McCauley, J. W., and Corbin, N. D., 1988, "Elastic Properties of Polycrystalline Aluminum Oxynitride Spinel and Their Dependence on Pressure, Temperature, and Composition," *J. Am. Ceram. Soc.*, **71**, pp. 807–812.
- [14] Zhang, K. S., Zhang, D., Feng, R., and Wu, M. S., 2005, "Microdamage in Polycrystalline Ceramics Under Dynamic Compression and Tension," *J. Appl. Phys.*, **98**, p. 023505.
- [15] Kraft, R. H., Molinari, J. F., Ramesh, K. T., and Warner, D. H., 2008, "Computational Micromechanics of Dynamic Compressive Loading of a Brittle Polycrystalline Material Using a Distribution of Grain Boundary Properties," *J. Mech. Phys. Solids*, **56**, pp. 2618–2641.
- [16] Foreman, A. J. E., 1955, "Dislocation Energies in Anisotropic Crystals," *Acta Metall.*, **3**, pp. 322–330.
- [17] Hirth, J. P., and Lothe, J., 1982, *Theory of Dislocations*, Wiley, New York.
- [18] Brace, W. F., Paulding, B. W., and Scholz, C., 1966, "Dilatancy in the Fracture of Crystalline Rocks," *J. Geophys. Res.*, **71**, pp. 3939–3953.
- [19] Clayton, J. D., 2008, "A Model for Deformation and Fragmentation in Crushable Brittle Solids," *Int. J. Impact Eng.*, **35**, pp. 269–289.
- [20] Graham, R. A., and Brooks, W. P., 1971, "Shock-Wave Compression of Sapphire From 15 to 420 kbar," *J. Phys. Chem. Solids*, **32**, pp. 2311–2330.
- [21] Grady, D. E., 1998, "Shock-Wave Compression of Brittle Solids," *Mech. Mater.*, **29**, pp. 181–203.
- [22] Clayton, J. D., 2010, "Deformation, Fracture, and Fragmentation in Brittle Geologic Solids," *Int. J. Fract.*, **163**, pp. 151–172.
- [23] Clayton, J. D., 2010, "Modeling Nonlinear Electromechanical Behavior of Shocked Silicon Carbide," *J. Appl. Phys.*, **107**, p. 013520.
- [24] Cazamias, J. U., Fiske, P. S., and Bless, S. J., 2001, "Shock Properties of AION," *Fundamental Issues and Applications of Shock-Wave and High-Strain-Rate Phenomena*, K. P. Staudhammer, L. E. Murr, and M. A. Meyers, eds., Elsevier, New York, pp. 181–188.
- [25] Vaughan, B. A. M., Proud, W. G., and Field, J. E., 2001, "Shock Properties of Aluminum Oxynitride," Cavendish Laboratory, Cambridge, UK, Report No. SP-1092.
- [26] Sekine, T., Li, X., Kobayashi, T., Yamashita, Y., Patel, P., and McCauley, J. W., 2003, "Aluminum Oxynitride at Pressures up to 180 GPa," *J. Appl. Phys.*, **94**, pp. 4803–4806.
- [27] Thornhill, T. F., Vogler, T. J., Rienhart, W. D., and Chhabildas, L. C., 2006, "Polycrystalline Aluminum Oxynitride Hugoniot and Optical Properties," *Shock Compression of Condensed Matter*, M. D. Furnish, M. Elert, T. P. Russell, and C. T. White, eds., American Institute of Physics, Melville, NY.
- [28] Lee, E. H., 1969, "Elastic-Plastic Deformation at Finite Strains," *ASME J. Appl. Mech.*, **36**, pp. 1–6.
- [29] Asaro, R. J., 1983, "Crystal Plasticity," *ASME J. Appl. Mech.*, **50**, pp. 921–934.
- [30] Thurston, R. N., 1974, "Waves in Solids," *Handbuch der Physik, Vol. VIa/4*, C. Truesdell, ed., Springer-Verlag, Berlin, pp. 109–308.
- [31] Clayton, J. D., 2009, "Modeling Effects of Crystalline Microstructure, Energy Storage Mechanisms, and Residual Volume Changes on Penetration Resistance of Precipitate-Hardened Aluminum Alloys," *Composites, Part B*, **40**, pp. 443–450.
- [32] Clayton, J. D., and Bammann, D. J., 2009, "Finite Deformations and Internal Forces in Elastic-Plastic Crystals: Interpretations From Nonlinear Elasticity and Anharmonic Lattice Statics," *ASME J. Eng. Mater. Technol.*, **131**, p. 041201.
- [33] Clayton, J. D., 2009, "A Non-Linear Model for Elastic Dielectric Crystals With Vacancies," *Int. J. Non-Linear Mech.*, **44**, pp. 675–688.
- [34] Mindlin, R. D., 1972, "Elasticity, Piezoelectricity, and Crystal Lattice Dynamics," *J. Elast.*, **2**, pp. 217–282.
- [35] Clayton, J. D., Chung, P. W., Grinfeld, M. A., and Nothwang, W. D., 2008, "Kinematics, Electromechanics, and Kinetics of Dielectric and Piezoelectric Crystals With Lattice Defects," *Int. J. Eng. Sci.*, **46**, pp. 10–30.
- [36] Li, H., Suematsu, H., Iseki, T., and Bradt, R. C., 1991, "Microhardness Anisotropy and the Indentation Load/Size Effect in $\text{MgO}-\text{xAl}_2\text{O}_3$ Single Crystals," *J. Ceram. Soc. Japan*, **99**, pp. 1079–1087.
- [37] Schäfer, H., Muller, W. F., and Hornemann, U., 1983, "Shock Effects in MgOAl_2O_3 -Spinel," *Phys. Chem. Miner.*, **9**, pp. 248–252.
- [38] Hornstra, J., 1960, "Dislocations, Stacking Faults and Twins in the Spinel Structure," *J. Phys. Chem. Solids*, **15**, pp. 311–323.
- [39] McCauley, J. W., 1978, "A Simple Model for Aluminum Oxynitride Spinel," *J. Am. Ceram. Soc.*, **61**, pp. 372–373.
- [40] Kocks, U. F., Argon, A. S., and Ashby, M. F., 1975, "Thermodynamics and Kinetics of Slip," *Prog. Mater. Sci.*, **19**, pp. 1–288.
- [41] Becker, R., 2004, "Effects of Crystal Plasticity on Materials Loaded at High Pressures and Strain Rates," *Int. J. Plast.*, **20**, pp. 1983–2006.
- [42] Christian, J. W., and Mahajan, S., 1995, "Deformation Twinning," *Prog. Mater. Sci.*, **39**, pp. 1–157.
- [43] Taylor, G. I., 1934, "The Mechanism of Plastic Deformation of Crystals," *Proc. R. Soc. London, Ser. A*, **145**, pp. 362–387.
- [44] Clayton, J. D., 2005, "Dynamic Plasticity and Fracture in High Density Polycrystals: Constitutive Modeling and Numerical Simulation," *J. Mech. Phys. Solids*, **53**, pp. 261–301.
- [45] Clayton, J. D., 2005, "Modeling Dynamic Plasticity and Spall Fracture in High Density Polycrystalline Alloys," *Int. J. Solids Struct.*, **42**, pp. 4613–4640.
- [46] Tressler, R. E., and Barber, D. J., 1974, "Yielding and Flow of C-Axis Sapphire Filaments," *J. Am. Ceram. Soc.*, **57**, pp. 13–19.
- [47] Daneu, N., Rečnik, A., Yamazaki, T., and Dolenec, T., 2007, "Structure and Chemistry of (111) Twin Boundaries in MgAl_2O_4 Spinel Crystals From Mogok," *Phys. Chem. Miner.*, **34**, pp. 233–247.
- [48] Mackenzie, J. K., 1950, "The Elastic Constants of a Solid Containing Spherical Holes," *Proc. Phys. Soc. London, Sect. B*, **63**, pp. 2–11.
- [49] Taylor, G. I., 1938, "Plastic Strain in Metals," *J. Inst. Met.*, **62**, pp. 307–324.
- [50] Kocks, U. F., 1970, "The Relation Between Polycrystal Deformation and Single Crystal Deformation," *Metall. Trans.*, **1**, pp. 1121–1143.
- [51] Wenk, H.-R., and Van Houtte, P., 2004, "Texture and Anisotropy," *Rep. Prog. Phys.*, **67**, pp. 1367–1428.
- [52] Schultz, R. A., Jensen, M. C., and Bradt, R. C., 1994, "Single Crystal Cleavage of Brittle Materials," *Int. J. Fract.*, **65**, pp. 291–312.
- [53] Mishra, R. K., and Thomas, G., 1977, "Surface Energy of Spinel," *J. Appl. Phys.*, **48**, pp. 4576–4580.
- [54] Steeds, J. W., 1973, *Introduction to Anisotropic Elasticity Theory of Dislocations*, Clarendon, Oxford.
- [55] Nabarro, F. R. N., 1947, "Dislocations in a Simple Cubic Lattice," *Proc. Phys. Soc. London*, **59**, pp. 256–272.
- [56] Eshelby, J. D., 1949, "Edge Dislocations in Anisotropic Materials," *Philos. Mag.*, **40**, pp. 903–912.

NO. OF
COPIES ORGANIZATION

1 DEFENSE TECHNICAL
(PDF INFORMATION CTR
only) DTIC OCA
8725 JOHN J KINGMAN RD
STE 0944
FORT BELVOIR VA 22060-6218

1 DIRECTOR
US ARMY RESEARCH LAB
IMNE ALC HRR
2800 POWDER MILL RD
ADELPHI MD 20783-1197

1 DIRECTOR
US ARMY RESEARCH LAB
RDRL CIM L
2800 POWDER MILL RD
ADELPHI MD 20783-1197

1 DIRECTOR
US ARMY RESEARCH LAB
RDRL CIM P
2800 POWDER MILL RD
ADELPHI MD 20783-1197

1 DIRECTOR
US ARMY RESEARCH LAB
RDRL D
2800 POWDER MILL RD
ADELPHI MD 20783-1197

ABERDEEN PROVING GROUND

1 DIR USARL
RDRL CIM G (BLDG 4600)

NO. OF
COPIES ORGANIZATION

ABERDEEN PROVING GROUND

30 DIR USARL
RDRL WM
J MCCAULEY
P PLOSTINS
RDRL WML B
I BATYREV
B RICE
N WEINGARTEN
RDRL WML H
B SCHUSTER
RDRL WMM B
G GAZONAS
RDRL WMP
S SCHOENFELD
RDRL WMP B
D CASEM
J CLAYTON (10 CPS)
D DANDEKAR
M GREENFIELD
C HOPPEL
R KRAFT
R LEAVY
B LOVE
M RAFTENBERG
T WEERASOORIYA
C WILLIAMS
RDRL WMP C
T BJERKE
RDRL WMP F
N GNIAZDOWSKI

INTENTIONALLY LEFT BLANK.